Continuous beam steering by coherent light-by-light control of dielectric metasurface phase gradient

Fei He,[1] Kevin F. MacDonald,[2] (iD) and Xu Fang[1,*] (iD)

[1]*School of Electronics and Computer Science, University of Southampton, SO17 1BJ, UK*
[2]*Optoelectronics Research Centre and Centre for Photonic Metamaterials, University of Southampton, SO17 1BJ, UK*
*x.fang@soton.ac.uk

Abstract: Continuous and reversible tuning of the properties of optical metasurfaces, as a functionality that would enable a range of device applications, has been a focus of the metasurface research field in recent years. Tuning mechanisms proposed and demonstrated so far have generally relied upon changing the morphology of a metasurface or the intrinsic properties of its constituent materials. Here we introduce, via numerical simulation, an alternative approach to achieve continuous tuning of gradient metasurface response, and illustrate its potential application to the challenge of continuous beam steering, as required for example in LIDAR and machine vision systems. It is based upon the coherent illumination of a silicon nano-pillar metasurface with two counter-propagating beams. Control of the input beams' relative phase and intensity enables tuning of the individual nano-pillars' electromagnetic response and thereby the phase gradient of the array, which in turn steers the direction of the output beam continuously over an angular range of approximately 9 degrees.

1. Introduction

Gradient index metasurfaces, ultrathin layers of artificial micro- and nano-structures, have opened up many novel approaches to manipulate light-matter interactions and to control the propagation and wavefront of light [1–3]. There has always been considerable interest in achieving active tuning of the properties of optical metamaterials and metasurfaces [4,5]. For many applications, e.g. light detection and ranging (LIDAR) and augmented reality, it is preferable that the tuning be truly continuous rather than incremental (i.e., proceeding through a limited number of discrete output state steps). One of the most widely explored approaches to achieving dynamic, volatile or non-volatile tuning is to utilize materials with intrinsic optical properties that are variable in response, for example, to heat, electrical bias or light intensity. Prior works in this category have used 2D materials (e.g., graphene and MoS_2) [6–8], media undergoing phase transition between two or more states (e.g. chalcogenides such as germanium antimony telluride, vanadium dioxide, and gallium) [9–12], doped semiconductors (e.g. indium tin oxide, silicon and gallium arsenide) [13–16], liquid crystals [17] and ionic conductors [18]. Another approach relies on structural deformation or reconfiguration of metasurfaces – the reversible adjustment of metamolecule shape and/or mutual positioning – through the use of flexible substrates or host matrices [19–22]. Both of these approaches depend on physical changes to the metasurface, either to the constituent materials or to the morphology of the array. Here, we present an approach that facilitates continuous tuning solely by changing the phase and intensity of illumination, without any change to either intrinsic material properties or the geometric configuration of the metasurface.

The functionality of a gradient metasurface is described by the generalized Snell's law [23]. It relates angles of incidence and reflection/refraction (θ_i and θ_r respectively) for light of vacuum wavelength λ_0 in media of refractive indices $n_{i,r}$ to the phase gradient $d\Phi/dx$ in the metasurface plane via:

$$n_r \sin(\theta_r) - n_i \sin(\theta_i) = \frac{\lambda_0}{2\pi} \frac{d\Phi}{dx} \tag{1}$$

On this basis, beam steering, defined as changing the output direction (θ_r) of an input beam at fixed wavelength (λ_0) and incident angle (θ_i), has previously been achieved by changing the electromagnetic environment ($n_{i,\,r}$) and the phase gradient ($d\Phi/dx$). Recent examples have explored utilizing field-effect modulation of free-carrier density [14], the optical contrast between the nematic and isotropic states of liquid crystal [24], and that between the amorphous and crystalline phases of chalcogenide glasses [25]. Here, we introduce the idea that $d\Phi/dx$ for a nanostructure of fixed geometry and material parameters can vary continuously, simply as a function of the incident electromagnetic field in the metasurface plane.

Our approach exploits the fact that the optical properties of subwavelength-thickness materials can manifest differently in travelling-wave and standing-wave electromagnetic fields. In general, they respond only to the *local* field [26]. In a standing field formed by two coherent, collinearly polarized counter-propagating incident beams, a sufficiently thin material (e.g., a metasurface) can be selectively addressed at the nodes/antinodes of electric (E) or magnetic (B) field formed by destructive/constructive interference (E nodes being necessarily coincident with B antinodes, and vice versa). 'Coherent control' in thin films and metamaterials has emerged in recent years as a powerful paradigm for manipulating all kinds of light-matter interactions with high contrast, high speed and low energy [26], and it presents a correspondingly broad range of technological opportunities from all-optical signal modulation [27] and image processing [28] to excitation-selective spectroscopy [29], including in the quantum regime [30].

The majority of applications considered thus far have relied upon the high (binary switching) contrast that is achievable between the limiting node and antinode configurations of coherent illumination [26,31,32]. In this work, we show how the full continuity of control over the electric and magnetic components of the excitation field in a metasurface plane, which is accessible in the coherent illumination regime, can be engaged for the purpose of all-optical, continuous θ_r sweeping.

2. Design of the beam-steering metasurface

Figure 1 shows a gradient metasurface design for coherently-controlled beam steering, which is comprised of an array of silicon nano-pillars on a semi-infinite glass substrate. Each unit cell contains a row of ten nano-pillars with a 300 nm center-to-center spacing along the x direction [Fig. 1(b)]. These unit cells form an infinite periodic array along the y direction at a periodicity $P = 300$ nm. Within each unit cell, the pillar height is fixed at $h = 160$ nm and diameters D increase in 6 nm steps from 120 nm to 174 nm in the $+x$ direction, to provide the illumination-dependent phase gradient $d\Phi/dx$, as will be discussed below. Note that the metasurface is of finite extent and not periodic in the x direction (i.e., the ten-pillar, 3 μm long unit cell does not repeat in this direction), because this would confine output light to a fixed set of discrete diffraction orders, eliminate the functionality of continuous beam steering.

The array is illuminated at normal incidence by a pair of counter-propagating beams (i.e., in the $\pm z$ directions) with collinear polarization in the x direction and a free-space wavelength $\lambda_0 = 555$ nm. In what follows, numerical simulations, which are conducted using a 3D finite-element Maxwell solver (COMSOL Multiphysics), take the complex refractive index of silicon from Ref. [33]. The value is $4.06 + 0.03i$ at λ_0. Following our recent work [34], the glass substrate is taken to be infinitely thick with a real refractive index of 1.5. For the two-beam illumination, the fields of the two incident waves are defined at the xy plane bisecting the pillars.
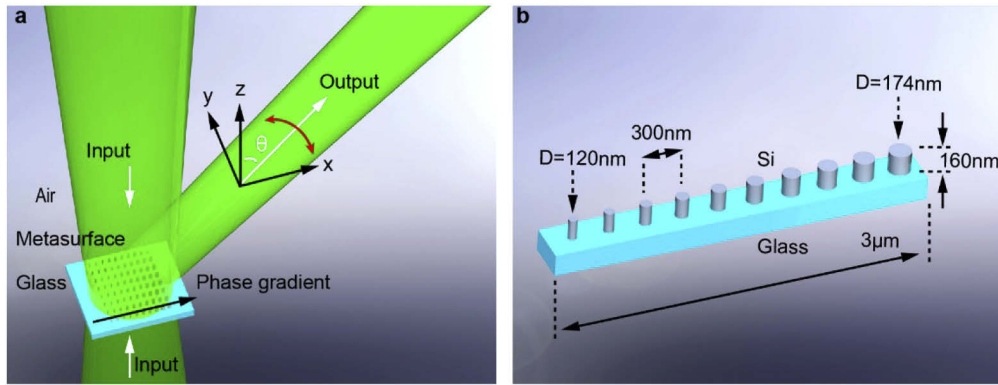
Fig. 1. Schematic illustration of a coherently controlled beam-steering metasurface. (a) The metasurface – an array of silicon nano-pillars on a semi-infinite glass substrate, with a phase gradient along the *x* direction – is illuminated by two coherent, *x*-polarized light beams at normal incidence. The primary output beam into free space (as opposed to the substrate) emerges at an oblique, tunable angle θ in the *xz* plane. For visualization, the semi-infinite substrate is shown as a slab with no output into it. (b) Each unit cell of the metasurface contains a row of ten silicon nano-pillars having equal height and center-to-center spacing, and a gradient of diameters.

In all cases, we account for the asymmetry of the metasurface environment (i.e., the presence of an optically thick glass substrate on one side and free space on the other, as would likely be the case in practical applications) as detailed in Ref. [34]. As will be discussed in details below, coherent illumination (i.e., modulating the relative phase and strength of the two incident beams) can modify the phase gradient *d*Φ*/dx* of the metasurface, resulting in continuous steering of the output beam by approximately 9°.

3. Optical response of arrays of identical nano-pillars

Development of the gradient metasurface design, as always, relies upon understanding of the scattering properties of the individual elements. To this end, we sequentially simulated the optical response of bi-periodic infinite square arrays of identical nano-pillars of fixed periodicity ($P = 300$ nm), fixed height ($h = 160$ nm) and varying diameter *D*. Figure 2 illustrates the case for $D = 120$ nm, the smallest nano-pillar in the metasurface. Figure 2(b) shows absorption spectra under coherent, standing-wave illumination with the E- or B-antinode at the plane bisecting the pillars at mid-height, together with the spectrum under single-beam (i.e., travelling-wave) illumination from the free-space side. The single-beam spectrum shows two absorption peaks at 510 and 580 nm. They are induced by Mie-type resonance modes of the nano-pillars [17], with the former approximating an electric dipole resonance and the latter a magnetic dipole resonance (see Fig. S1 in the Supplementary for near-field analysis). This attribution is confirmed by the fact that under coherent illumination at the E-antinode, where electric field strength is doubled and magnetic field is zero at the middle plane of the nano-pillar, the 510 nm (electric) resonance is enhanced and the 580 nm (magnetic) resonance is suppressed, and vice versa at the B-antinode. In both cases, the suppressed peak does not disappear completely, as the nano-pillar slightly deviates from an ideal, zero-thickness resonator due to its finite height.

For the purpose of continuously tunable beam steering, we are interested in the variation of scattering properties between the limiting cases of E- and B- antinodes, as shown in Fig. 2(c). In consideration of the directional asymmetry arising from the presence of an optically thick substrate on one side of the nano-pillar array, the tuning range is represented by the magnetic
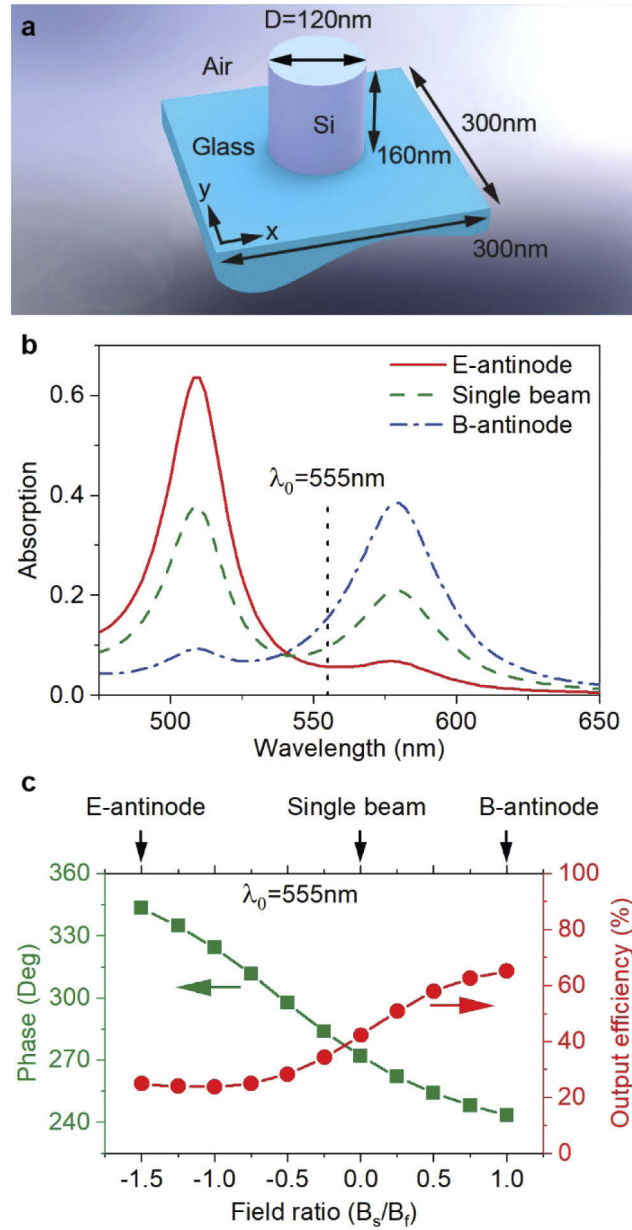
Fig. 2. Optical properties of a bi-periodic, square array of identical pillars. (a) Dimensional schematic of a unit cell. (b) Absorption spectra under double-beam (standing wave with the E- and B-antinodes at the array) and single-beam (travelling wave incident from the free-space side) illumination. The absorption is computed relative to the total input power in each case. (c) Efficiency (relative to total input power) and phase (relative to the free-space input beam) of output scattering into free space (in the $+z$ direction) as a function of illumination condition, denoted by the magnetic field ratio of substrate and free-space incident beams (B_s and B_f, respectively). The value B_s/B_f is taken at the plane bisecting the pillars at mid-height. The wavelength is 555 nm, the design wavelength of the gradient metasurface.

field ratio of the substrate and free-space incident beams (B_s and B_f, respectively) at the array plane (electric field ratio could equally be used). The sign of B_s/B_f corresponds to the relative phase between the two incident beams, while its amplitude corresponds to their relative strength. On this scale [Fig. 2(c)], E- and B- antinodes at the array plane occur at B_s/B_f ratios of -1.5 and 1.0, respectively, and the illumination condition of a single beam from free space is found at $B_s/B_f = 0$ (i.e., zero substrate beam field). Here and in what follows, while there are output plane waves propagating in both the $+z$ and $-z$ directions, we specifically consider the output beam into free space ($+z$), as it is more likely to be harnessed in device applications.

The dependence of scattering phase on illumination condition B_s/B_f is a key parameter in the gradient metasurface design. It is defined here relative to the free-space incident beam (e.g., it would be π for a single beam reflected from an air-glass interface). Meanwhile, output efficiency [Fig. 2(c)] is defined as the ratio of power in the free space output beam to the total power of both input beams. For simple and effective coherent control, one is seeking a scattering phase that varies monotonically, preferably linearly, with illumination condition B_s/B_f, accompanied by little, preferably zero, variation in output efficiency. For the present example of a nano-pillar with
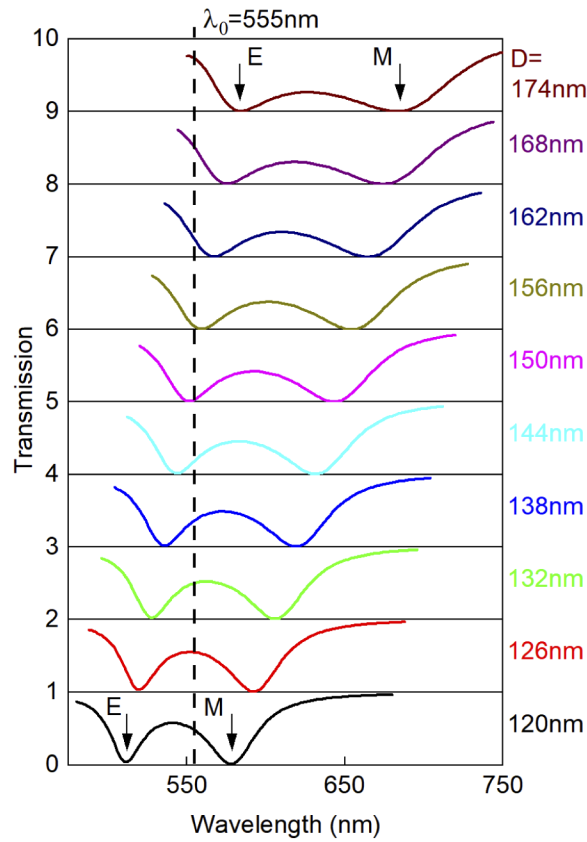

Fig. 3. Single-beam transmission of infinite square arrays of silicon nano-pillars on a semi-infinite glass substrate, with periodicity $P = 300$ nm, pillar height $h = 160$ nm, and diameter D ranging from 120 to 174 nm (as labelled). The arrays are illuminated at normal incidence. Spectra are vertically offset with a step of transmission = 1 for clarity. The vertical dashed line denotes $\lambda_0 = 555$ nm, the design wavelength of the gradient metasurface. Electric and magnetic resonances are indicated by E and M labels against spectra for the smallest and largest pillars, and they shift monotonically with D.

$D = 120$ nm, we obtain a phase tuning range of 243° - 343° with a close-to-linear dependence upon B_s/B_f, together with an approximately sigmoidal variation of efficiency between 24% and 65% (see Fig. S2 for a comparison among the different energy output channels).

The same analysis is performed on a range of nano-pillar diameters up to $D = 174$ nm. Over this range, the pillars' optical response is characterized generically by the same combination of an electric and a magnetic resonance as shown for the $D = 120$ nm case in Fig. 2, with the resonance wavelengths increasing with pillar diameter D. This is illustrated in Fig. 3 on the basis of single-beam transmission spectra which, in accordance with the requirements of linear reciprocity, are identical for the two opposing directions of normal propagation relevant to the present study. Importantly from the perspective of gradient metasurface design, while the magnetic resonance wavelength is longer than the metasurface design wavelength ($\lambda_0 = 555$ nm) for all nano-pillar diameters, the electric resonance wavelength is $<\lambda_0$ for smaller pillar diameters and $>\lambda_0$ for larger diameters (crossing over between $D = 150$ and 156 nm).

From this analysis of bi-periodic arrays, Fig. 4(a) shows dependence of output beam phase at $\lambda_0 = 555$ nm on both nano-pillar diameter D and illumination condition B_s/B_f. The field ratio B_s/B_f ranges from the E- to the B-antinode, and the points between 243° and 343° along the phase curve of Fig. 2(c) correspond to the left hand end points of the family of curves here in Fig. 4(a). Aside from some deviations for the largest and smallest pillars in the limiting E and B-antinodal regimes, the dependences of phase upon pillar diameter are close to linear across most of the nano-pillar diameter range, with gradients decreasing monotonically from E- to B-antinode illumination. Interestingly, the lines converge to a single point between $D = 150$ and 156 nm where phase $\sim\pi$. This is a consequence of the fact that single-beam transmission of λ_0 is zero at this point (Fig. 3). Coherent excitation relies upon the interference of two counter-propagating incident light waves, but zero transmission eliminates this interference, rendering the metasurface
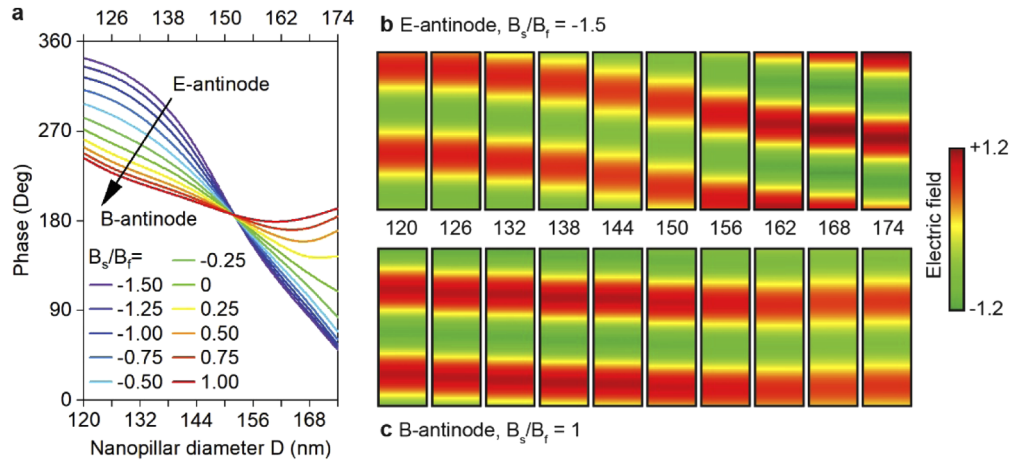

Fig. 4. Output phase at λ_0 for different nano-pillar diameters and illumination conditions. (a) Dependence on pillar diameter D of output beam phase for infinite square arrays of silicon nano-pillars. The arrays have the same periodicity $P = 300$ nm and pillar height $h = 160$ nm, and they are under a range of coherent illumination conditions B_s/B_f from the E- to the B-antinode (as labelled). (b, c) Corresponding output electric field distributions in the xz plane from 1 to 3 μm above the plane bisecting the nano-pillars, under (b) the E-antinode and (c) the B-antinode coherent illumination. The pillar diameter D ranges from 120 to 174 nm. All the maps show a plane wave that propagates in the $+z$ direction, with its field independent of the x position. Field strength is normalized to that of the free-space input beam, which is a constant for all the cases.

insensitive to the relative phase and intensity of a second beam. The ~π phase shift observed at this point demonstrates that, the response of these nano-pillars is a very good approximation to that of a subwavelength array of resonant electric dipoles.

Figures 4(b) and 4(c) further show the scattered electric field for each nano-pillar diameter in the limiting-cases of the E- and B-antinodes. At the E-antinode [B_s/B_f = -1.5, Fig. 4(b)], phase retardation depends strongly upon nano-pillar diameter, increasing monotonically with D. In contrast, at the B-antinode [B_s/B_f = 1.0, Fig. 4(c)], there is very little phase difference across the entire range of diameters. This behavior can be understood from Fig. 3. Under the E-antinode illumination, the behavior of the arrays is governed entirely by the electric resonance, because the magnetic resonance is suppressed. As shown in Fig. 3, as D increases from 120 nm to 174 nm, the wavelength of the electric resonance moves across the λ_0 = 555 nm line. For a dipole resonator, this regime of resonance shift maximizes output phase dispersion with pillar diameter. By comparison, under the B-antinode illumination, the behavior of the arrays is governed by the magnetic resonance (the electric resonance being suppressed) and the operating wavelength λ_0 is always shorter than the resonance wavelength. As such, output phase is relatively insensitive to D.

4. Beam steering characteristics

From Fig. 4, it is apparent that a metasurface in which unit cells contain a size gradient of silicon nano-pillars, as illustrated in Fig. 1(b), can provide a continuously tunable phase gradient under coherent illumination. This behavior is illustrated in Fig. 5(b), which shows the output field above the gradient metasurface for the E-antinode (B_s/B_f = -1.5), the B-antinode (B_s/B_f = 1.0), and a selection of intermediate B_s/B_f values. The metasurface provides continuous tuning of output beam angle in the xz plane, i.e. parallel to the structurally engineered phase gradient along the x direction. (There is no variation of nano-pillar diameter and therefore no phase gradient along y, consequently no angular deflection in the yz plane.) The wavefront is seen to remain nearly flat in all cases (a perfectly flat wavefront is actually forbidden by the limited x-direction size of the metasurface) and specular reflection/transmission of the two incident beams (strictly in the $+z$ direction) is essentially eliminated. The angular intensity distributions [Fig. 5(c)] show that output light is concentrated almost entirely in a single lobe. Output beam angle θ, defined as that of maximum output intensity, changes continuously from 10.6° at the E-antinode to 1.5° at the B-antinode, giving a steering range of 9.1°.

Output beam angle is plotted as a function of B_s/B_f at the metasurface plane (Fig. 6). Values derived as above from finite element numerical simulation are well-matched to an analytical estimate based on the generalized Snell's law [Eq. (1)]. The latter assumes that the nano-pillars provide a linear phase gradient $d\Phi/dx$ [given simply by the phase difference between the smallest (D = 120 nm) and largest (D = 174 nm) pillars at all the B_s/B_f field ratios, and their center-to-center spatial separation of 9×300 nm = 2.7 μm], and that they have equal scattering efficiencies. It also excludes any influence of near-field coupling among nano-pillars. As such, its close match to the numerical data shows that such coupling is relatively weak in the present case (thereby validating the assumption that gradient metasurface performance can very reasonably be evaluated from knowledge of the individual resonator characteristics [3]). As a consequence, the beam steering functionality is only weakly dependent on the incident polarization (angular tuning range for y-polarized light is from 1.7 to 10.5°). Figure 6 also shows beam steering efficiency, defined as power scattered into the primary output beam lobe relative to total input power, varies between 26% and 46% in the whole range of B_s/B_f (as distinct to the +/-z scattering efficiency considered in Fig. 2).
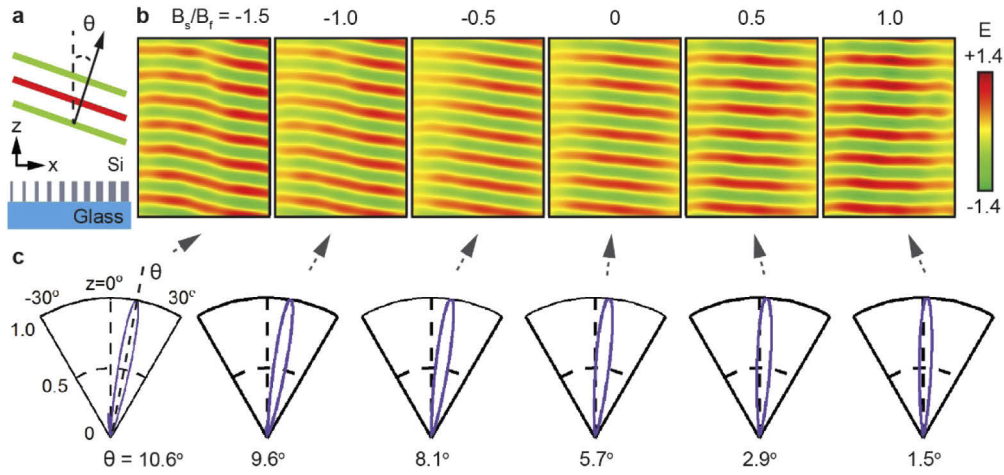
Fig. 5. Coherently controlled beam steering metasurface. (a) Simplified schematic cross-section of the nano-pillar gradient metasurface (see details in Fig.1) in the *xz* steering plane. (b) Output electric field distributions in the *xz* plane from 1 to 5 μm above the middle plane of the metasurface for selected coherent illumination conditions (as labelled). Each sub-panel is 3 μm wide, i.e. the width of the 10-pillar gradient unit cell shown in Fig. 1(b). Field strength is normalized to that of the free-space input beam, which is a constant for all the cases. (c) Corresponding angular distributions of output intensity, each normalized to their respective maxima.
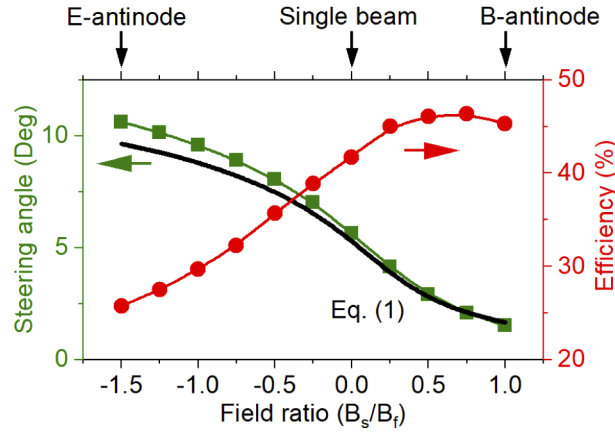

Fig. 6. Steering angle and efficiency. Output beam angle θ and beam steering efficiency (relative to total input power) of the phase gradient metasurface as functions of input field ratio B_s/B_f. The symbols represent values obtained from numerical simulations of the whole gradient metasurface, while the solid black line is an analytical estimate based on Eq. (1) and the simulated phases of the largest and smallest nano-pillars.

5. Conclusion

The coherent control concept is scalable across wavebands from optical to THz with appropriate selection of material platform and resonator geometry (e.g., see Fig. S3 for a design working at the telecomm wavelength of 1550 nm). For the implementation of the proposed beam steering concept, any of the oxides, nitrides and semiconductors typically employed in all-dielectric metasurfaces would be suitable (e.g., GaN, TiO_2, ZnO, Te and SiN [35–38]): the medium need

not to be dissipative (as silicon is at visible wavelengths) - indeed lower intrinsic losses would improve output efficiency; and the resonators do not have to be cylindrical - the basic requirement is that they support electric and magnetic resonances at closely spaced wavelengths. As long as the two resonances exhibit significant dispersion contrast at the operating wavelength (e.g., either the electric or the magnetic resonance is highly dispersive), the phase gradient of the metasurface, and therefore output beam angle, can be coherently tuned.

To conclude, we have introduced the concept of a coherently controllable dielectric metasurface phase gradient, and further demonstrated its application to continuous beam steering at visible wavelengths, by using an array of silicon nano-pillars with a fixed gradient of diameters. Under illumination by a pair of coherent, collinearly polarized, counter-propagating input beams, the output beam from the metasurface can be swept smoothly over a range of 9.1° as a function of the relative phase and intensity of the two inputs. The beam steering originates from the fact that, the coherent interference of the two input beams controls the electric and magnetic dipolar responses of each nano-pillar. As such, the nano-pillars collectively present a phase gradient that continuously maps the relative phase and intensity of the incident beams onto output beam angle.

Funding

Data availability

Following a period of embargo from the date of publication, the data that support the findings will be available in the University of Southampton's ePrints research repository.

Disclosures

The authors declare no conflicts of interest.

See Supplement 1 for supporting content.

References

1. H. T. Chen, A. J. Taylor, and N. F. Yu, "A review of metasurfaces: physics and applications," Rep. Prog. Phys. **79**(7), 076401 (2016).
2. S. B. Glybovski, S. A. Tretyakov, P. A. Belov, Y. S. Kivshar, and C. R. Simovski, "Metasurfaces: From microwaves to visible," Phys. Rep. **634**, 1–72 (2016).
3. S. M. Kamali, E. Arbabi, A. Arbabi, and A. Faraon, "A review of dielectric optical metasurfaces for wavefront control," Nanophotonics **7**(6), 1041–1068 (2018).
4. A. M. Shaltout, V. M. Shalaev, and M. L. Brongersma, "Spatiotemporal light control with active metasurfaces," Science **364**(6441), eaat3100 (2019).
5. Q. He, S. L. Sun, and L. Zhou, "Tunable/Reconfigurable Metasurfaces: Physics and Applications," Research **2019**, 1–16 (2019).
6. N. Dabidian, I. Kholmanov, A. B. Khanikaev, K. Tatar, S. Trendafilov, S. H. Mousavi, C. Magnuson, R. S. Ruoff, and G. Shvets, "Electrical Switching of Infrared Light Using Graphene Integration with Plasmonic Fano Resonant Metasurfaces," ACS Photonics **2**(2), 216–227 (2015).
7. B. B. Zeng, Z. Q. Huang, A. Singh, Y. Yao, A. K. Azad, A. D. Mohite, A. J. Taylor, D. R. Smith, and H. T. Chen, "Hybrid graphene metasurfaces for high-speed mid-infrared light modulation and single-pixel imaging," Light: Sci. Appl. **7**(1), 51 (2018).
8. P. N. Ni, A. D. Bugallo, V. M. A. Arreola, M. F. Salazar, E. Strupiechonski, V. Brandli, R. Sawant, B. Alloing, and P. Genevet, "Gate-Tunable Emission of Exciton-Plasmon Polaritons in Hybrid MoS$_2$-Gap-Mode Metasurfaces," ACS Photonics **6**(7), 1594–1601 (2019).
9. J. Rensberg, S. Zhang, Y. Zhou, A. S. McLeod, C. Schwarz, M. Goldflam, M. K. Liu, J. Kerbusch, R. Nawrodt, S. Ramanathan, D. N. Basov, F. Capasso, C. Ronning, and M. A. Kats, "Active Optical Metasurfaces Based on Defect-Engineered Phase-Transition Materials," Nano Lett. **16**(2), 1050–1055 (2016).

10. R. F. Waters, P. A. Hobson, K. F. MacDonald, and N. I. Zheludev, "Optically switchable photonic metasurfaces," Appl. Phys. Lett. **107**(8), 081102 (2015).

11. M. R. M. Hashemi, S. H. Yang, T. Y. Wang, N. Sepulveda, and M. Jarrahi, "Electronically-Controlled Beam-Steering through Vanadium Dioxide Metasurfaces," Sci. Rep. **6**(1), 35439 (2016).

12. M. Wuttig, H. Bhaskaran, and T. Taubner, "Phase-change materials for non-volatile photonic applications," Nat. Photonics **11**(8), 465–476 (2017).

13. A. Howes, W. Y. Wang, I. Kravchenko, and J. Valentine, "Dynamic transmission control based on all-dielectric Huygens metasurfaces," Optica **5**(7), 787–792 (2018).

14. Y. W. Huang, H. W. H. Lee, R. Sokhoyan, R. A. Pala, K. Thyagarajan, S. Han, D. P. Tsai, and H. A. Atwater, "Gate-Tunable Conducting Oxide Metasurfaces," Nano Lett. **16**(9), 5319–5325 (2016).

15. K. B. Fan, J. D. Zhang, X. Y. Liu, G. F. Zhang, R. D. Averitt, and W. J. Padilla, "Phototunable Dielectric Huygens' Metasurfaces," Adv. Mater. **30**(22), 1800278 (2018).

16. Y. C. Jun, J. Reno, T. Ribaudo, E. Shaner, J. J. Greffet, S. Vassant, F. Marquier, M. Sinclair, and I. Brener, "Epsilon-Near-Zero Strong Coupling in Metamaterial-Semiconductor Hybrid Structures," Nano Lett. **13**(11), 5391–5396 (2013).

17. J. Sautter, I. Staude, M. Decker, E. Rusak, D. N. Neshev, I. Brener, and Y. S. Kivshar, "Active Tuning of All-Dielectric Metasurfaces," ACS Nano **9**(4), 4308–4315 (2015).

18. K. Thyagarajan, R. Sokhoyan, L. Zornberg, and H. A. Atwater, "Millivolt Modulation of Plasmonic Metasurface Optical Response via Ionic Conductance," Adv. Mater. **29**(31), 1701044 (2017).

19. S. M. Kamali, E. Arbabi, A. Arbabi, Y. Horie, and A. Faraon, "Highly tunable elastic dielectric metasurface lenses," Laser Photonics Rev. **10**(6), 1002–1008 (2016).

20. H. S. Ee and R. Agarwal, "Tunable Metasurface and Flat Optical Zoom Lens on a Stretchable Substrate," Nano Lett. **16**(4), 2818–2823 (2016).

21. P. Cencillo-Abad, E. Plum, E. T. F. Rogers, and N. I. Zheludev, "Spatial optical phase-modulating metadevice with subwavelength pixelation," Opt. Express **24**(16), 18790–18798 (2016).

22. A. She, S. Y. Zhang, S. Shian, D. R. Clarke, and F. Capasso, "Adaptive metalenses with simultaneous electrical control of focal length, astigmatism, and shift," Sci. Adv. **4**(2), eaap9957 (2018).

23. N. F. Yu, P. Genevet, M. A. Kats, F. Aieta, J. P. Tetienne, F. Capasso, and Z. Gaburro, "Light Propagation with Phase Discontinuities: Generalized Laws of Reflection and Refraction," Science **334**(6054), 333–337 (2011).

24. A. Komar, R. Paniagua-Dominguez, A. Miroshnichenko, Y. F. Yu, Y. S. Kivshar, A. I. Kuznetsov, and D. Neshev, "Dynamic Beam Switching by Liquid Crystal Tunable Dielectric Metasurfaces," ACS Photonics **5**(5), 1742–1748 (2018).

25. C. R. de Galarreta, A. M. Alexeev, Y. Y. Au, M. Lopez-Garcia, M. Klemm, M. Cryan, J. Bertolotti, and C. D. Wright, "Nonvolatile Reconfigurable Phase-Change Metadevices for Beam Steering in the Near Infrared," Adv. Funct. Mater. **28**(10), 1704993 (2018).

26. E. Plum, K. F. MacDonald, X. Fang, D. Faccio, and N. I. Zheludev, "Controlling the Optical Response of 2D Matter in Standing Waves," ACS Photonics **4**(12), 3000–3011 (2017).

27. X. Fang, K. F. MacDonald, and N. I. Zheludev, "Controlling light with light using coherent metadevices: all-optical transistor, summator and invertor," Light: Sci. Appl. **4**(5), e292 (2015).

28. M. Papaioannou, E. Plum, and N. I. Zheludev, "All-Optical Pattern Recognition and Image Processing on a Metamaterial Beam Splitter," ACS Photonics **4**(2), 217–222 (2017).

29. X. Fang, M. L. Tseng, D. P. Tsai, and N. I. Zheludev, "Coherent Excitation-Selective Spectroscopy of Multipole Resonances," Phys. Rev. Appl. **5**(1), 014010 (2016).

30. A. Lyons, D. Oren, T. Roger, V. Savinov, J. Valente, S. Vezzoli, N. I. Zheludev, M. Segev, and D. Faccio, "Coherent metamaterial absorption of two-photon states with 40% efficiency," Phys. Rev. A **99**(1), 011801 (2019).

31. J. H. Shi, X. Fang, E. T. F. Rogers, E. Plum, K. F. MacDonald, and N. I. Zheludev, "Coherent control of Snell's law at metasurfaces," Opt. Express **22**(17), 21051–21060 (2014).

32. S. Kita, K. Takata, M. Ono, K. Nozaki, E. Kuramochi, K. Takeda, and M. Notomi, "Coherent control of high efficiency metasurface beam deflectors with a back partial reflector," APL Photonics **2**(4), 046104 (2017).

33. M. A. Green, "Self-consistent optical parameters of intrinsic silicon at 300 K including temperature coefficients," Sol. Energy Mat. Sol. C **92**(11), 1305–1310 (2008).

34. F. He, K. F. MacDonald, and X. Fang, "Coherent illumination spectroscopy of nanostructures and thin films on thick substrates," Opt. Express **26**(10), 12415–12423 (2018).

35. S. Liu, M. B. Sinclair, T. S. Mahony, Y. C. Jun, S. Campione, J. Ginn, D. A. Bender, J. R. Wendt, J. F. Ihlefeld, P. G. Clem, J. B. Wright, and I. Brener, "Optical magnetic mirrors without metals," Optica **1**(4), 250–256 (2014).

36. W. T. Chen, A. Y. Zhu, V. Sanjeev, M. Khorasaninejad, Z. J. Shi, E. Lee, and F. Capasso, "A broadband achromatic metalens for focusing and imaging in the visible," Nat. Nanotechnol. **13**(3), 220–226 (2018).

37. S. M. Wang, P. C. Wu, V. C. Su, Y. C. Lai, M. K. Chen, H. Y. Kuo, B. H. Chen, Y. H. Chen, T. T. Huang, J. H. Wang, R. M. Lin, C. H. Kuan, T. Li, Z. L. Wang, S. N. Zhu, and D. P. Tsai, "A broadband achromatic metalens in the visible," Nat. Nanotechnol. **13**(3), 227–232 (2018).

38. S. Colburn, A. Zhan, and A. Majumdar, "Metasurface optics for full-color computational imaging," Sci. Adv. **4**(2), eaar2114 (2018).